ACS Photonics
pubs.acs.org/journal/apchd5 Article

Spatially Resolved Magnetic-Field-Induced Intensity Modulation Enhancement under the Goos–Hänchen Effect in Magnetophotonic Crystals

Anastasia A. Nerovnaya,[§] Aleksandr Yu. Frolov,[§] and Andrey A. Fedyanin*

Cite This: *ACS Photonics* 2026, 13, 3501–3508 Read Online

ACCESS | Metrics & More | Article Recommendations | Supporting Information

ABSTRACT: The magnetic-field-induced modulation of the spatially resolved reflected light intensity in one-dimensional magnetophotonic crystals (MPCs) under the Goos–Hänchen (GH) effect is observed. The excitation of Bloch surface waves in MPCs leads to the GH effect manifesting as the appearance of a second reflected beam shifted by 50.5λ relative to the specular one. Applying a magnetic field in a polar configuration induces the conversion of transverse electric Bloch surface waves into transverse magnetic waves that propagate into the far field. This modulates the spatial distribution of the reflected light intensity being obtained under the GH shift in MPCs with a modulation value of up to 19.6%. The observed values are 2 orders of magnitude higher than the conventionally measured modulation based on the intensity changes of the total reflected light beam.

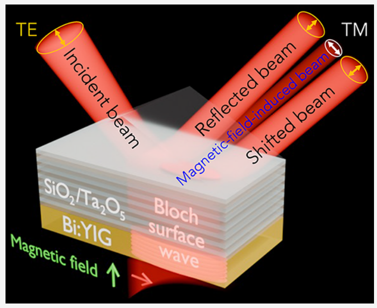

KEYWORDS: *magnetophotonic crystals, Goos–Hänchen effect, Bloch surface waves, magneto-optical effect, magnetic dielectrics, magneto-optical modulation*

■ INTRODUCTION

The high sensitivity of resonant optical effects in nanophotonic structures to external stimuli may significantly expand the possibilities for active control of light properties. One notable example of these phenomena is the Goos–Hänchen (GH) effect, also known as the Goos–Hänchen shift, involving a lateral displacement of the reflected beam along the interface in comparison with the position predicted by geometric optics.[1,2] Typically, the GH shift remains limited to only a few wavelengths of incident light in the case of dielectric interfaces and metal surfaces[3] due to the low field localization of evanescent waves. However, the GH effect can be enhanced up to several hundreds of incident light wavelengths by the excitation of propagating surface plasmons[4] in thin metal films,[5] plasmonic crystals,[6,7] metamaterials,[8,9] and metasurfaces.[10] Dielectric nanostructures have low optical losses and thus enable even greater enhancement of the GH effect through the excitation of Bloch surface waves (BSWs) and defect modes in photonic crystals,[11−17] unidirectional guided modes in photonic crystal slabs,[18,19] as well as bound states in the continuum in all-dielectric metasurfaces.[20−24] The GH effect in these resonant optical structures is sensitive to external conditions, thus allowing for tunability achieved through the application of electric fields,[25,26] thermal heating,[27] and optical pumping.[28] Incorporating magnetic materials into the resonant optical structures makes it possible to use a magnetic field for remote and ultrafast control of resonance features.[29−38] Enhanced magnetic-field-induced changes in light intensity and polarization, known as the magneto-optical Kerr and Faraday effects, have been observed in both magnetoplasmonic[39−49] and magnetophotonic[50−60] structures. Integrating magnetic materials into resonant photonic architectures also provides an effective route for a dynamic tuning of the Goos–Hänchen effect, offering control over its magnitude and direction under external magnetic fields.[61−70] Recently, it was shown that the spatially resolved transverse magneto-optical Kerr effect associated with the GH shift in nickel magnetoplasmonic crystals exceeds the conventionally measured value by 2.6 times.[71] Despite their advantages, ferromagnetic magnetoplasmonic crystals suffer from high absorption, which limits the electromagnetic field penetration into the magnetic medium and suppresses the achievable magnitude of magneto-optical effects. In these systems, the field is predominantly localized at the surface of the magnetic material, restricting its interaction with the volume. In contrast, one-dimensional magnetophotonic crystals (MPCs) represent the optically transparent resonant structures defined by low losses. MPCs are typically photonic crystals complemented by magnetic dielectric materials. A magnetic layer may be embedded into a photonic crystal as a defect layer or act as one of the materials in a pair of layers.[72−75] It is also possible

Received: March 27, 2026
Revised: May 25, 2026
Accepted: May 29, 2026
Published: June 8, 2026

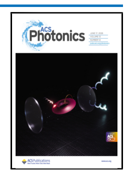

https://doi.org/10.1021/acsphotonics.6c00737
ACS Photonics 2026, 13, 3501−3508

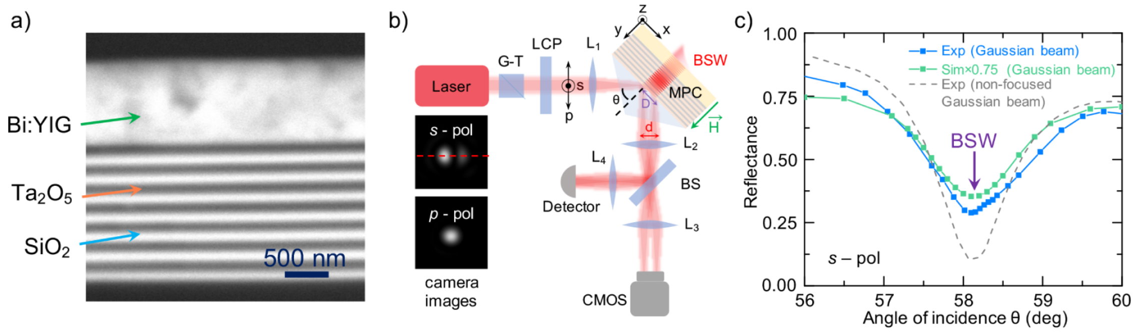

Figure 1. (a) The SEM image of the MPC slice. (b) Schematic of the experimental setup for measuring the angular dependences of the reflectance, the GH effect, and the spatially resolved magnetic-field-induced modulation of reflected light intensity in the MPC. CMOS camera images of reflected light at $\theta = 58.1°$ under *s* (top) and *p* (bottom) polarizations are shown on the left side of the experimental setup. The experimental intensity cross-sections in Figure 2 were taken along the red dashed line on the CMOS image. (c) Experimental (blue dots) and simulated (green dots) angular dependence of the MPC reflectance in the case of the focused Gaussian incident beam with *s*-polarization. The gray dashed curve shows the experimental angular reflectance of the MPC observed with unfocused *s*-polarized incident laser diode radiation.

for the magnetic layer to border the surface of a photonic crystal. Such MPCs support either BSWs, also called optical Tamm states,[76] that propagate at their interface, or localized defect modes. Both BSWs and defect modes exhibit a long-time interaction and high field localization in the magnetic layers, providing high tunability of the near-field intensity and polarization when an external magnetic field is applied. This significantly boosts the magneto-optical Kerr and Faraday effects in MPCs.[77−80] However, the benefits of the spatial resolution of the magnetic-field-induced intensity modulation under the presence of the GH effect in MPCs have not yet been revealed.

In this work, we experimentally and numerically demonstrate the magnetic-field-induced modulation of the spatial intensity distribution associated with the GH shift in the MPC. The excitation of the Bloch surface waves gives rise to the GH effect, which manifests itself as two reflected beams spatially shifted relative to each other. Applying an external magnetic field to the MPCs in a polar configuration significantly modulates the spatial intensity distribution of the reflected beams under the GH effect. The magnetic-field-induced modulation of the spatial intensity distribution in the MPCs exceeds the value of the modulation observed in the conventional measurements that include the intensity changes of the total reflected beam.

■ RESULTS AND DISCUSSION

Sample, Experimental Setup, and Simulations

Figure 1a shows the SEM image of an MPC slice. The MPC consists of 7 pairs of SiO_2 and Ta_2O_5 layers with bismuth-substituted yttrium iron garnet (Bi:YIG) on top. The thicknesses of the layers are 130 nm, 90 nm, and 1060 nm, respectively.

The scheme of the experimental setup is shown in Figure 1b. Light from a laser diode (CPS670F from Thorlabs) with a wavelength of $\lambda = 675$ nm passes through a Glan−Taylor prism (G-T) and a liquid crystal plate (LCP, LCC1113-A from Thorlabs), generating either *s*- or *p*-polarized beams by a liquid crystal controller (LCC25 from Thorlabs). After passing through a lens (L1) with a focal length of $f = 30$ mm, the light propagates through a right BK7 glass prism and a layer of immersion oil, focusing on the MPC surface. This enables the excitation of BSWs in the Kretschmann configuration.[78] The focused laser beam is approximated by a Gaussian function with a beam waist of 10 μm. After reflection from the sample, the beam passes through a magnifying system consisting of two lenses: L2 with $f = 13$ mm and L3 with $f = 125$ mm. The spatial intensity distribution of the reflected beam is detected by a CMOS camera (DCC1545M from Thorlabs). The 50:50 nonpolarized beam splitter between lenses L2 and L3 delivers light to the Si-detector (DET36A/M from Thorlabs), which measures the total intensity of the reflected beam. A static external magnetic field is applied to the MPC in polar configuration (along the *y*-axis) using a servo rotation stage with a fixed neodymium magnet. The magnetic field strength is equal to 1500 G at the position of the focused beam. To change the angle of the incident light (θ), the laser, G-T, LCP, and L1 were fixed on the one arm of the goniometer while the glass prism with the MPC was mounted on the other. The Si-detector and the CMOS camera were not rotated. The goniometer consists of two rotation stages from Sigma-Koki that allow for a 0.1° step of the incident light angle.

To simulate the angular dependence of the MPC reflectance and the intensity cross-section of the reflected beams, the finite-difference time-domain method (Ansys Lumerical FDTD) was used.[81] A Gaussian beam with a central wavelength of 675 nm, a beam waist of 10 μm, and an angular divergence of 0.9° was used as a light source. To take into account the narrow spectral line of the laser diode radiation, the reflectance and intensity cross-sections were calculated as average values at 674.9 nm, 675 nm, and 675.1 nm for each incident angle of light. A monitor that detects the total MPC reflection and the reflected intensity cross-section at a particular incident angle was placed above the source. Both the source and the monitor were placed into a glass substrate with a refractive index of 1.51. The model of the MPC consisted of 7 pairs of SiO_2 and Ta_2O_5 layers with thicknesses of 132 and 93 nm, respectively. The refractive indices were 1.46 and 2.1, respectively. The layer on top of the periodic structure has a thickness of 1059 nm, a refractive index of $n = 2.21$, and an extinction coefficient of $\kappa = 0.0014$. The latter was taken into account for the scattering of light on the inhomogeneities of the Bi:YIG layer. The modulation of the reflected light intensity under an external magnetic field in polar configuration was simulated by implementing anisotropy into the dielectric permittivity tensor of the Bi:YIG layer. The anisotropic dielectric permittivity tensor of Bi:YIG has the following components:

$$\hat{\varepsilon} = \begin{pmatrix} \varepsilon & 0 & ig \\ 0 & \varepsilon & 0 \\ -ig & 0 & \varepsilon \end{pmatrix} \quad (1)$$

where $\varepsilon = (n + i\kappa)^2$. The off-diagonal components are $\varepsilon_{xz} = ig$ and $\varepsilon_{zx} = -ig$, where g is the gyration constant of Bi:YIG. The value of the Bi:YIG gyration constant is $g = 0.0035$ at $\lambda = 675$ nm.[82]

MPC Reflectance

The experimental (blue dots) and the simulated (green dots) angular dependences of the MPC reflectance are shown in Figure 1c for an incident focused Gaussian beam with *s*-polarization. To achieve visual agreement between the experimental and the simulated results, the simulated curve was multiplied by a factor of 0.75 that includes unaccounted reflections from the faces of the prism in the simulations. The minimum reflectance observed for both curves at an incident angle of $\theta = 58.1°$ indicates the excitation of a BSW. There are no resonant features in the MPC reflectance for the *p*-polarized incident Gaussian beam in this range of angles. Focusing of the incident radiation broadens the resonance line width. The intrinsic line width of the resonance, shown by a gray dashed curve, was measured without focusing L1 and objective L2 lenses. The angular width of the resonance is approximately 1°, which is comparable to the divergence of the focused incident beam.

GH Effect in MPC

Two camera images in Figure 1b show the spatial distribution of the *p*- and the *s*-polarized reflected beams at $\theta = 58.1°$ corresponding to the minimum of angular reflectance for *s*-polarization. In the case of *p*-polarized incident light, there is only a spot associated with the beam specularly reflected from the MPC, whereas for the *s*-polarized incident light, the camera image has two spots, indicating the GH effect. The left spot arises from the nonresonant specularly reflected beam, while the right one is associated with the excitation and propagation of the BSW. The GH shift is defined as the distance (D) between the maxima of the reflected intensity along the plane of the MPC surface (see Figure 1b). The experimental cross-section of the beams along their centers (along x-axis in the xy-plane) at a resonant angle of 58.1° is shown in Figure 2a by the green curve. The GH shift is equal to $D = 34.1$ μm (50.5λ). The red curve in Figure 2a demonstrates the simulated intensity cross-section $I(x)$ of the reflected beam at a resonant angle of 58.1° corresponding to BSW excitation. The simulated value of the GH shift equals $D = 34.8$ μm (51.5λ). To clearly show the appearance of the two reflected beams, we simulated a two-dimensional electric field distribution $|E(x,y)|$ (Figure 2b) at a wavelength of 675 nm and an incident angle of $\theta = 58.1°$. This demonstrates that the incident Gaussian beam excites the BSW in the MPC layers, which propagates along the MPC surface (x-axis). Six electric field antinodes within the Bi:YIG layer indicate the excitation of the sixth-order transverse electric (TE) BSW. The resonant excitation of the BSW causes high field localization, which splits the reflected beam into two: the left beam reflects from the MPC surface as if it was a mirror, and the right one undergoes a lateral shift along the interface, revealing a GH shift with a value D between the maxima along the plane of the MPC surface.

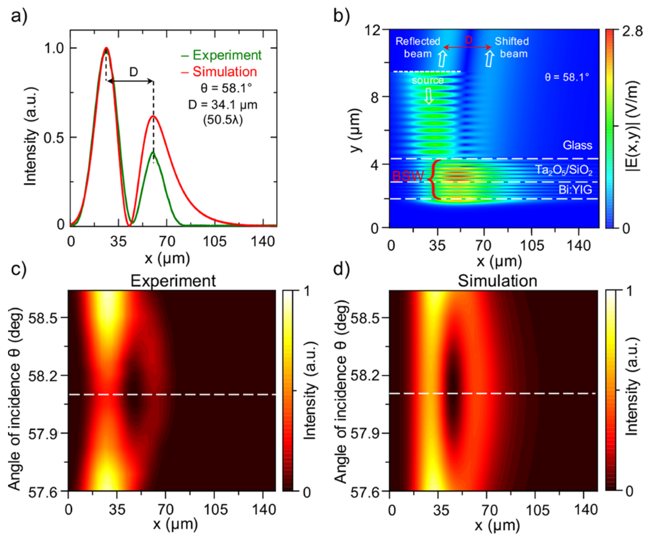

Figure 2. (a) Experimental (green curve) and simulated (red curve) intensity cross-sections of the *s*-polarized beam reflected from the MPC under resonant excitation of the BSW ($\theta = 58.1°$). (b) Simulation of the spatial electric field distribution $|E(x,y)|$ under the GH effect in the MPC. (c) Experimental and (d) simulated angular dependences of the intensity cross-section of the *s*-polarized beam reflected from the MPC. The dashed horizontal lines in (c) and (d) correspond to the intensity cross-sections in (a).

Angular Dependence of the GH Effect

The map in Figure 2c shows the angular dependence of the intensity cross-section of camera images along the centers of the reflected beams. Two separated intensity maxima indicate the appearance of the GH effect. They are observed near the light incident angle corresponding to the BSW excitation ($57.7° < \theta < 58.5°$). When the incident angle is outside of the resonant range ($\theta \geq 58.5°$ and $\theta \leq 57.8°$), there is only one maximum, which indicates the disappearance of the GH effect. The simulated angular dependence of the intensity cross-sections of the reflected light in Figure 2d exhibits a similar trend to the one experimentally observed. The dashed white lines on both maps correspond to the intensity cross-sections in Figure 2a, with the maximum GH effect being equal to $D = 34.1$ μm (50.5λ) in the experiment and $D = 34.8$ μm (51.5λ) in the simulations. The comparison of the experimental and simulated angular dependences of the GH effect, obtained from the intensity cross-section, is presented in Figure S1 of the Supporting Information (SI1). Figure S2 in the Supporting Information (SI2) shows the angular dependence of the GH effect, calculated using the phase-stationary method with a plane wave as an incident light source.

Modulation of the Spatial Intensity Distribution under the GH Effect

The schematic of the magnetic-field-induced modulation of the spatial intensity distribution of the reflected beam under the GH effect is illustrated in Figure 3a. To modulate the spatial intensity distribution of the reflected light from the MPC under the GH effect, a magnetic field is applied in a polar configuration (along the y-axis) as shown in Figure 3a. The appearance of the off-diagonal terms ε_{xz} and ε_{zx} in the Bi:YIG dielectric permittivity tensor converts the E_z component of the TE BSW into E_x and E_y components. As MPC does not support any resonant transverse magnetic (TM) BSWs at this wavelength and incident angle, the converted light propagates

https://doi.org/10.1021/acsphotonics.6c00737
ACS Photonics 2026, 13, 3501−3508

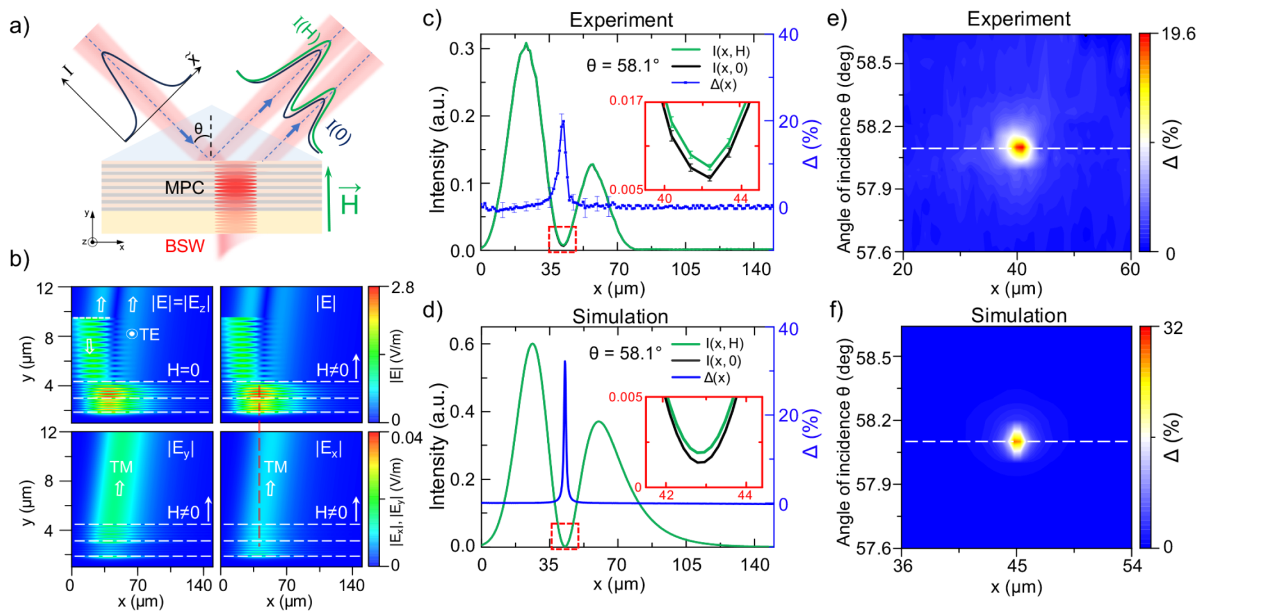

Figure 3. (a) The schematic of the magnetic-field-induced modulation of the spatial intensity distribution under the GH effect in the MPC. (b) The top two images correspond to the simulations of $|E(x,y)|$ without and with a magnetic field. The bottom two images show $|E_x(x, y)|$ and $|E_y(x,y)|$ components induced by a magnetic field in polar configuration. (c) Experimental and (d) simulated intensity cross-sections $I(x,H)$ (green curve) and $I(x, 0)$ (black curve), measured at the resonant angle with and without an external magnetic field, respectively. Blue curves represent the spatially resolved magnetic-field-induced modulation $\Delta(x)$ of the reflected light intensity. (e) Experimental and (f) simulated angular dependences of $\Delta(x)$ in the MPC. The dashed lines correspond to $\Delta(x)$ shown in (c) and (d).

into the far-field as a TM wave. This process is illustrated in Figure 3b by simulations of electric field distributions. The TM-polarized beam with $|E_x|$ and $|E_y|$ components (two bottom images) appears under the magnetic field in a polar configuration. It is generated from the BSW TE electric field localized into the Bi:YIG layer and propagates into the far-field. This TE to TM mode conversion underlines the modulation in the spatial distribution of the reflected beam's intensity. To measure the modulation magnitude, we record the spatial intensity cross-section of the reflected beam with $I(x,H)$ and without $I(x,0)$ the magnetic field H. The value of the modulation is defined by the following equation:

$$\Delta(x) = \frac{I(x, H) - I(x, 0)}{I(x, H) + I(x, 0)} \times 200\% \qquad (2)$$

$\Delta(x)$ represents the average of the 50 individual $\Delta(x)$ measurements. Figure 3c shows the cross-sections of the reflected beam intensity with ($I(x,H)$, green curve) and without ($I(x,0)$, black curve) the magnetic field at a resonant incident angle of $\theta = 58.1°$. The difference in the intensity cross-sections with and without the magnetic field, shown in the inset in Figure 3c, clearly demonstrates the magnetic-field-induced modulation in the vicinity of the intensity minimum. The blue dots ($\Delta(x)$) represent the quantitative difference between the two spatial intensity distributions. The maximum modulation in the experiment is equal to $\Delta(x) = 19.6 \pm 1.5\%$. Moreover, it is observed at the minimum of the intensity cross-sections $I(x,H)$ and $I(x,0)$. The minimum value of the spatial distribution of intensity corresponds to the area of the highest electric field localization associated with BSW excitation in MPC layers (see Figures 2b and 3b). Therefore, the highest $\Delta(x)$ location is near the minimum of the reflected intensity, as the magnetic field induces TE to TM mode conversion, which increases with field localization inside the magnetic layer.

Figure 3e depicts the experimental angular dependence of $\Delta(x)$ over the range $57.6° < \theta < 58.6°$. The white dashed line corresponds to the maximum value of $\Delta(x)$ cross-section, which is depicted in Figure 3c. The value of $\Delta(x)$ decreases rapidly to zero if the incident angle deviates from $\theta = 58.1°$.

The simulation results of $\Delta(x)$ qualitatively coincide with the experimental ones. Figure 3d shows that the maximum magnitude of the spatial intensity modulation (blue curve) at the resonant angle of $\theta = 58.1°$ equals to $\Delta(x) = 32.2\%$ and lies near the minimum of the intensity cross-sections (black and green curves). Figure 3f also demonstrates the maximum $\Delta(x)$ value at the incident angles where the GH effect occurs. The differences between the maximum values of the experimental and simulated $\Delta_{max}(x)$ can be attributed to the presence of surface roughness in Bi:YIG, different values of the gyration constant g of Bi:YIG, and differences in the spectral width of the incident radiation. Figure S3 in the Supporting Information (SI3) shows simulations of $\Delta(x)$ curves for various values of gyration constants. $\Delta(x)$ increases with increasing ε_{xz} and ε_{zx} values. It should be noted that the enhancement of $\Delta(x)$ is accompanied by an enhancement in the absolute magnetic-field-induced modulation of the spatial distribution of intensity, $\Delta I(x) = I(x,H) - I(x,0)$, which can be seen in Figure S4 in the Supporting Information (SI4). The highest maximum of $\Delta I(x)$ occurs near the position where the field is localized in the Bi:YIG layer, due to the excitation of the BSW wave.

Comparison of Magnetic-Field-Induced Spatially Resolved Intensity Modulation Δ(x) and Full Intensity Modulation Δ

The advantage of spatially resolving the magnetic-field-induced intensity modulation under the GH effect becomes evident when compared to the modulation conventionally obtained from the total reflected beam. The latter is defined by the following equation:

https://doi.org/10.1021/acsphotonics.6c00737
ACS Photonics 2026, 13, 3501−3508

$$\Delta = \frac{I(H) - I(0)}{I(H) + I(0)} \times 200\% \quad (3)$$

where the $I(H)$ and $I(0)$ are the overall intensities ($I(H)$ and $I(0) \sim \int I(x,z)\mathrm{d}x\mathrm{d}z$) of the reflected beam with and without an external magnetic field, respectively. The experimental angular dependences of the reflectance (pink square dots) and Δ (blue open dots) are shown in Figure 4a. The corresponding simulations are demonstrated in Figure 4b. The simulation conditions were the same as those for the spatial intensity distribution under the GH effect. As the simulation was performed in a two-dimensional area (xy-plane), $I(H)$ and $I(0)$ are therefore proportional to the integral of the spatial intensity distribution along the x-axis ($I(H)$ and $I(0) \sim \int I(x)\mathrm{d}x$). The maximum Δ is observed in the vicinity of the MPC reflectance minimum for both the experiment and the simulations. The blue filled dots in Figure 4a and b indicate the angular dependences of $\Delta(x)$, taken at the x-coordinate corresponding to its maximum values (x = 40.4 μm in the experiment and x = 45 μm in the simulations). The maximum experimental value is equal to Δ = 0.08%, which is 245 times less than the maximum of the spatially resolved value $\Delta_{max}(x)$ = 19.6%. The simulated value of Δ is 0.06%. It is 537 times less than $\Delta_{max}(x)$ = 32.2%, which qualitatively coincides with the experimental results. Thus, the observed magnetic-field-induced modulation of the spatial intensity distribution under the GH effect significantly exceeds the conventional one.[39−60]

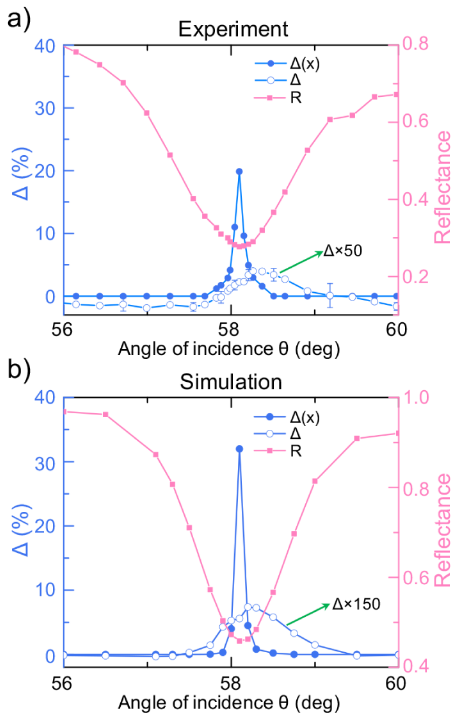

Figure 4. (a) Experimental and (b) simulated angular dependence of the MPC reflectance (pink square dots) and Δ (blue open dots) calculated integrally over the whole reflected beam without spatial resolution. The blue filled dots in panels (a) and (b) show the angular dependence of the spatially resolved reflected intensity modulation values $\Delta(x)$ taken at x-coordinates corresponding to its maximum values.

■ CONCLUSION

In conclusion, we have experimentally demonstrated the presence of the GH effect in one-dimensional magneto-photonic crystals, which leads to the appearance of two reflected beams separated by a distance D. At the resonant excitation of Bloch surface waves, the GH shift reached up to D = 34.1 μm (50.5λ). Moreover, under an external magnetic field in polar configuration, the spatial intensity distribution under the GH effect is significantly modified due to the conversion of a TE BSW to TM waves. The maximum modulation observed in the experiment was $\Delta(x)$ = 19.6% at the position of maximum field localization, where the minimum intensity occurred between the two reflected beams. In comparison with the conventionally measured modulation of the total reflected beam, the maximum of the spatially resolved modulation $\Delta(x)$ is 245 times higher. Therefore, these findings can advance the sensitivity of magneto-optical sensors and the performance of magneto-optical modulators.

■ ASSOCIATED CONTENT

Supporting Information

The Supporting Information is available free of charge at https://pubs.acs.org/doi/10.1021/acsphotonics.6c00737.

SI1: Experimental and simulated angular dependence of the GH shift. SI2: Simulation of the GH shift using the phase stationary method. SI3: Spatially resolved magnetic-field-induced intensity modulation under the GH shift, depending on the magnetization of the Bi:YIG layer. SI4: Spatially resolved magnetic-field-induced absolute intensity modulation $\Delta I(x) = I(x,H) - I(x,0)$ under the GH effect (PDF)

■ AUTHOR INFORMATION

Corresponding Author

Andrey A. Fedyanin − *Lomonosov Moscow State University, Moscow 119991, Russia;* orcid.org/0000-0003-4708-6895; Email: fedyanin@nanolab.phys.msu.ru

Authors

Anastasia A. Nerovnaya − *Shenzhen MSU-BIT University, Shenzhen 517182, China; Lomonosov Moscow State University, Moscow 119991, Russia*

Aleksandr Yu. Frolov − *Shenzhen MSU-BIT University, Shenzhen 517182, China; Lomonosov Moscow State University, Moscow 119991, Russia;* orcid.org/0000-0003-0988-1361

Complete contact information is available at: https://pubs.acs.org/10.1021/acsphotonics.6c00737

Author Contributions

§A.A.N. and A.Y.F. contributed equally to this work

Funding

This study was supported by the Russian Science Foundation (grant no. 24-72-00042).The reported study in part of calculations is funded by Shenzhen Municipal Government and Shenzhen MSU-BIT University.

Notes

The authors declare no competing financial interest.

■ ACKNOWLEDGMENTS

A.Y.F. thanks the Russian Science Foundation (grant no. 24-72-00042) for supporting the experimental measurements and simulations. The study was conducted under the state assignment of Lomonosov Moscow State University. A.A.N. acknowledges the Foundation for the Advancement of Theoretical Physics and Mathematics “BASIS” for the scholarship award. The authors would like to express their gratitude to Prof. Mitsuteru Inoue, Dr. Alexander I. Musorin, and Dr. Irina V. Soboleva for providing the magnetophotonic crystal and for the useful discussions. The authors would like to thank Maria S. Gavrushina for her assistance in conducting the experiment and Margarita I. Sharipova for providing the SEM image of the magnetophotonic crystal.

■ REFERENCES

(1) Goos, F.; Hänchen, H. Ein neuer und fundamentaler Versuch zur Totalreflexion. *Ann. Phys.* **1947**, *436*, 333−346.
(2) Renard, R. H. Total reflection: a new evaluation of the Goos−Hänchen shift. *J. Opt. Soc. Am.* **1964**, *54*, 1190−1197.
(3) Merano, M.; Aiello, A.; Hooft, G. W.; van Exter, M. P.; Eliel, E. R.; Woerdman, J. P. Observation of Goos-Hänchen shifts in metallic reflection. *Opt. Express* **2007**, *15* (24), 15928−15934.
(4) Barnes, W. L.; Dereux, A.; Ebbesen, T. W. Surface plasmon subwavelength optics. *Nature* **2003**, *424*, 824−830.
(5) Yin, X.; Hesselink, L.; Liu, Z.; Fang, N.; Zhang, X. Large positive and negative lateral optical beam displacements due to surface plasmon resonance. *Appl. Phys. Lett.* **2004**, *85*, 372−374.
(6) Bonnet, C.; Chauvat, D.; Emile, O.; Bretenaker, F.; Le Floch, A.; Dutriaux, L. Measurement of positive and negative Goos-Hänchen effects for metallic gratings near Wood anomalies. *Opt. Lett.* **2001**, *26*, 666−668.
(7) Petrov, N. I.; Danilov, V. A.; Popov, V. V.; Usievich, B. A. Large positive and negative Goos-Hänchen shifts near the surface plasmon resonance in subwavelength grating. *Opt. Express* **2020**, *28*, 7552−7564.
(8) He, J.; Yi, J.; He, S. Giant negative Goos-Hänchen shifts for a photonic crystal with a negative effective index. *Opt. Express* **2006**, *14*, 3024−3029.
(9) Xu, Y.; Chan, C. T.; Chen, H. Goos-Hänchen effect in epsilon-near-zero metamaterials. *Sci. Rep.* **2015**, *5* (1), 8681.
(10) Liu, Y.; Chang, Z.; Zhang, C.; Cai, J.; Yu, H.; Liu, N.; Wu, H.; Jiang, S.; Guo, C.; Wu, J. Giant Goos-Hänchen shift by steering the transition from local to nonlocal plasmonic resonances. *Opt. Lett.* **2026**, *51*, 445−448.
(11) Yeh, P.; Yariv, A.; Cho, A. Y. Optical surface waves in periodic layered media. *Appl. Phys. Lett.* **1978**, *32*, 104−104.
(12) Soboleva, I. V.; Moskalenko, V. V.; Fedyanin, A. A. Giant Goos-Hänchen effect and Fano resonance at photonic crystal surfaces. *Phys. Rev. Lett.* **2012**, *108*, 123901.
(13) Wang, L.-G.; Zhu, S.-Y. Giant lateral shift of a light beam at the defect mode in one-dimensional photonic crystals. *Opt. Lett.* **2006**, *31*, 101−103.
(14) Felbacq, D.; Moreau, A.; Smaâli, R. Goos-Hänchen effect in the gaps of photonic crystals. *Opt. Lett.* **2003**, *28*, 1633−1635.
(15) Paul, T.; Rockstuhl, C.; Menzel, C.; Lederer, F. Resonant Goos-Hänchen and Imbert-Fedorov shifts at photonic crystal slabs. *Phys. Rev. A* **2008**, *77*, 053802.
(16) Du, S.; Zhang, W.; Liu, W.; Zhang, Y.; Zhao, M.; Shi, L. Realization of large transmitted optical Goos-Hänchen shifts in photonic crystal slabs. *Nanophotonics* **2022**, *11*, 4531−4536.
(17) Wong, Y.-P.; Miao, Y.; Skarda, J.; Solgaard, O. Large negative and positive optical Goos-Hänchen shift in photonic crystals. *Opt. Lett.* **2018**, *43*, 2803−2806.
(18) Gong, M.; Zhang, Z.; Tu, Q.; Hu, P.; Peng, C.; Gao, Z. Giant Goos−Hänchen Shift with Stable High-Efficiency Emission Enabled by Topological High-Q Unidirectional Guided Resonances. *ACS Photonics* **2025**, *12*, 5464−5471.
(19) Wu, Z.; Zhen, W.; Ren, Z.-C.; Wang, X.-L.; Wang, H.-T.; Ding, J. Controlling Enhancement of Transmitted Goos-Hänchen Shifts: From Symmetric to Unidirectional. *Laser Photonics Rev.* **2026**, *20* (2), No. e01398.
(20) Wu, F.; Wu, J.; Guo, Z.; Jiang, H.; Sun, Y.; Li, Y.; Ren, J.; Chen, H. Giant enhancement of the Goos-Hänchen shift assisted by quasibound states in the continuum. *Phys. Rev. Appl.* **2019**, *12*, 014028.
(21) Zheng, Z.; Zhu, Y.; Duan, J.; Qin, M.; Wu, F.; Xiao, S. Enhancing Goos-Hänchen shift based on magnetic dipole quasi-bound states in the continuum in all-dielectric metasurfaces. *Opt. Express* **2021**, *29*, 29541−29549.
(22) Qi, X.; Wu, J.; Wu, F.; Ren, M.; Wei, Q.; Guo, Z.; Jiang, H.; Chen, Y.; Yang, Y.-P.; Chen, H.; Sun, Y. Topologically enabled giant angle-insensitive Goos-Hänchen shift by tunable merging bound states in the continuum of a quasiflat band. *Phys. Rev. B* **2024**, *110*, 035420.
(23) Sinha Biswas, S.; Remesh, G.; Achanta, V. G.; Banerjee, A.; Ghosh, N.; Dutta Gupta, S. Enhanced beam shifts mediated by bound states in continuum. *J. Optics* **2023**, *25*, 095401.
(24) Qi, X.; Wu, J.; Guo, Z.; Jiang, H.; Yang, Y.; Wu, F.; Chen, H.; Sun, Y. Tailoring Photonic Dispersion via Multiple Brillouin Zone Foldings: A Route From Robust Ultrahigh-Q Resonances Toward Robust Giant Goos-Hänchen Shifts. *Laser Photonics Rev.* **2026**, No. e02879.
(25) Wang, Y.; Cao, Z.; Li, H.; Hao, J.; Yu, T.; Shen, Q. Electric control of spatial beam position based on the Goos-Hänchen effect. *Appl. Phys. Lett.* **2008**, *93* (9), 091103.
(26) Sun, D. A proposal for digital electro-optic switches with free-carrier dispersion effect and Goos-Hänchen shift in silicon-on-insulator waveguide corner mirror. *J. Appl. Phys.* **2013**, *114* (10), 104502.
(27) Yu, B.; Tang, T.; Wang, R.; Qiao, S.; Li, Y.; Li, C.; Shen, J.; Huang, X.; Cao, Y. Magneto-optical and thermo-optical modulations of Goos-Hänchen effect in one-dimensional photonic crystal with graphene-VO2. *J. Magn. Magn. Mater.* **2021**, *530*, 167946.
(28) Emile, O.; Galstyan, T.; Le Floch, A.; Bretenaker, F. Measurement of the Nonlinear Goos-Hänchen Effect for Gaussian Optical Beams. *Phys. Rev. Lett.* **1995**, *75*, 1511−1513.
(29) Vabishchevich, P. P.; Frolov, A. Y.; Shcherbakov, M. R.; Grunin, A. A.; Dolgova, T. V.; Fedyanin, A. A. Magnetic field-controlled femtosecond pulse shaping by magnetoplasmonic crystals. *J. Appl. Phys.* **2013**, *113*, 17A947.
(30) Shcherbakov, M. R.; Vabishchevich, P. P.; Frolov, A. Y.; Dolgova, T. V.; Fedyanin, A. A. Femtosecond intrapulse evolution of the magneto-optic Kerr effect in magnetoplasmonic crystals. *Phys. Rev. B* **2014**, *90*, 201405.
(31) Novikov, I. A.; Kiryanov, M. A.; Frolov, A. Y.; Popov, V. V.; Dolgova, T. V.; Fedyanin, A. A. Spatially Inhomogeneous Ultrafast Demagnetization of a Nickel Magnetoplasmonic Crystal. *JETP Lett.* **2023**, *118*, 574−578.
(32) Novikov, I. A.; Kiryanov, M. A.; Nurgalieva, P. K.; Frolov, A. Y.; Popov, V. V.; Dolgova, T. V.; Fedyanin, A. A. Ultrafast Magneto-Optics in Nickel Magnetoplasmonic Crystals. *Nano Lett.* **2020**, *20*, 8615−8619.
(33) Fan, Y.; Cao, G.; Jiang, S.; Åkerman, J.; Weissenrieder, J. Spatiotemporal observation of surface plasmon polariton mediated ultrafast demagnetization. *Nat. Commun.* **2025**, *16* (1), 873.
(34) Mishra, K.; Rowan-Robinson, R. M.; Ciuciulkaite, A.; Davies, C. S.; Dmitriev, A.; Kapaklis, V.; Kimel, A. V.; Kirilyuk, A. Ultrafast Demagnetization Control in Magnetophotonic Surface Crystals. *Nano Lett.* **2022**, *22*, 9773−9780.
(35) Alekhin, A.; Lomonosov, A. M.; Leo, N.; Ludwig, M.; Vlasov, V. S.; Kotov, L.; Leitenstorfer, A.; Gaal, P.; Vavassori, P.; Temnov, V. Quantitative Ultrafast Magnetoacoustics at Magnetic Metasurfaces. *Nano Lett.* **2023**, *23*, 9295−9302.

(36) Xu, H.; Hajisalem, G.; Steeves, G. M.; Gordon, R.; Choi, B. C. Nanorod Surface Plasmon Enhancement of Laser-Induced Ultrafast Demagnetization. *Sci. Rep.* **2015**, *5* (1), 15933.

(37) Sidiropoulos, T.; Singh, P.; Noll, T.; Schneider, M.; Engel, D.; Sommer, D.; Steinbach, F.; Will, I.; Pfau, B.; von Korff Schmising, C.; Eisebitt, S. Subwavelength Localized All-Optical Helicity-Independent Magnetic Switching Using Plasmonic Gold Nanostructures. *Nano Lett.* **2025**, *25*, 4645−4651.

(38) Kazlou, A.; Chekhov, A. L.; Stognij, A. I.; Razdolski, I.; Stupakiewicz, A. Surface Plasmon-Enhanced Photomagnetic Excitation of Spin Dynamics in Au/YIG: Co Magneto-Plasmonic Crystals. *ACS Photonics* **2021**, *8*, 2197−2202.

(39) Grunin, A. A.; Zhdanov, A. G.; Ezhov, A. A.; Ganshina, E. A.; Fedyanin, A. A. Surface-plasmon-induced enhancement of magneto-optical Kerr effect in all-nickel subwavelength nanogratings. *Appl. Phys. Lett.* **2010**, *97*, 261908.

(40) Armelles, G.; Cebollada, A.; García-Martín, A.; González, M. U. Magnetoplasmonics: combining magnetic and plasmonic functionalities. *Adv. Opt. Mater.* **2013**, *1*, 10−35.

(41) Ferguson, P. E.; Stafsudd, O. M.; Wallis, R. F. Enhancement of the transverse Kerr magneto-optic effect by surface magnetoplasma waves. *Physica B+C* **1977**, *89*, 91−94.

(42) Clavero, C.; Yang, K.; Skuza, J.; Lukaszew, R. Magnetic field modulation of intense surface plasmon polaritons. *Opt. Express* **2010**, *18*, 7743−7752.

(43) Maccaferri, N.; Gabbani, A.; Pineider, F.; Kaihara, T.; Tapani, T.; Vavassori, P. Magnetoplasmonics in confined geometries: Current challenges and future opportunities. *Appl. Phys. Lett.* **2023**, *122*, 120502.

(44) López-Ortega, A.; Zapata-Herrera, M.; Maccaferri, N.; Pancaldi, M.; Garcia, M.; Chuvilin, A.; Vavassori, P. Enhanced magnetic modulation of light polarization exploiting hybridization with multipolar dark plasmons in magnetoplasmonic nanocavities. *Light: Sci. Appl.* **2020**, *9* (1), 49.

(45) Frolov, A. Y.; Shcherbakov, M. R.; Fedyanin, A. A. Dark mode enhancing magneto-optical Kerr effect in multilayer magnetoplasmonic crystals. *Phys. Rev. B* **2020**, *101*, 045409.

(46) Kiryanov, M. A.; Frolov, A. Y.; Novikov, I. A.; Kipp, P. A.; Nurgalieva, P. K.; Popov, V. V.; Ezhov, A. A.; Dolgova, T. V.; Fedyanin, A. A. Surface profile-tailored magneto-optics in magnetoplasmonic crystals. *APL Photonics* **2022**, *7*, 026104.

(47) Kataja, M.; Hakala, T. K.; Julku, A.; Huttunen, M. J.; van Dijken, S.; Törmä, P. Surface lattice resonances and magneto-optical response in magnetic nanoparticle arrays. *Nat. Commun.* **2015**, *6*, 7072.

(48) Borovkova, O. V.; Kozhaev, M. A.; Hashim, H.; Kolosova, A. A.; Kalish, A. N.; Dagesyan, S. A.; Shaposhnikov, A. N.; Berzhansky, V. N.; Belotelov, V. I. Transverse magneto-photonic transmission effect in non-symmetric nanostructures with comb-like plasmonic gratings. *Optical Mater. Express* **2022**, *12*, 573−583.

(49) Cheng, T.-H.; Yang, W.; Sun, S.; Liu, Z.; Feng, H. Y.; Qin, J.; Bi, L.; Luo, F. Magnetoplasmonic Gratings Induced an Unusual Magneto-Optical Kerr Effect at Optical Frequencies. *Laser Photonics Rev.* **2025**, *19* (5), 2401476.

(50) Barsukova, M. G.; Shorokhov, A. S.; Musorin, A. I.; Neshev, D. N.; Kivshar, Y. S.; Fedyanin, A. A. Magneto-Optical Response Enhanced by Mie Resonances in Nanoantennas. *ACS Photonics* **2017**, *4*, 2390−2395.

(51) Barsukova, M. G.; Musorin, A. I.; Shorokhov, A. S.; Fedyanin, A. A. Enhanced magneto-optical effects in hybrid Ni-Si metasurfaces. *APL Photonics* **2019**, *4*, 016102.

(52) Chernyak, A. M.; Barsukova, M. G.; Shorokhov, A. S.; Musorin, A. I.; Fedyanin, A. A. Bound States in the Continuum in Magnetophotonic Metasurfaces. *JETP Lett.* **2020**, *111*, 46−49.

(53) Ignatyeva, D. O.; Karki, D.; Voronov, A. A.; Kozhaev, M. A.; Krichevsky, D. M.; Chernov, A. I.; Levy, M.; Belotelov, V. I. All-dielectric magnetic metasurface for advanced light control in dual polarizations combined with high-Q resonances. *Nat. Commun.* **2020**, *11* (1), 5487.

(54) Carvalho, W. O. F.; Mejía-Salazar, J. R. All-dielectric magnetophotonic gratings for maximum TMOKE enhancement. *Phys. Chem. Chem. Phys.* **2022**, *24*, 5431−5436.

(55) Bsawmaii, L.; Gamet, E.; Royer, F.; Neveu, S.; Jamon, D. Longitudinal magneto-optical effect enhancement with high transmission through a 1D all-dielectric resonant guided mode grating. *Opt. Express* **2020**, *28*, 8436−8444.

(56) Bsawmaii, L.; Gamet, E.; Neveu, S.; Jamon, D.; Royer, F. Magnetic nanocomposite films with photo-patterned 1D grating on top enable giant magneto-optical intensity effects. *Optical Mater. Express* **2022**, *12*, 513−523.

(57) Voronov, A. A.; Karki, D.; Ignatyeva, D. O.; Kozhaev, M. A.; Levy, M.; Belotelov, V. I. Magneto-optics of subwavelength all-dielectric gratings. *Opt. Express* **2020**, *28*, 17988−17996.

(58) Carvalho, W. O. F.; Filho, M. T. A. T.; Oliveira, O. N., Jr; Mejía-Salazar, J. R.; de Figueiredo, F. A. P. Toward Machine-Learning-Accelerated Design of All-Dielectric Magnetophotonic Nanostructures. *ACS Appl. Mater. Interfaces* **2024**, *16* (32), 42828−42834.

(59) Mamian, K. A.; Popov, V. V.; Frolov, A. Y.; Fedyanin, A. A. Tailoring transverse magneto-optical Kerr effect enhancement in Mie-resonant nanowire-based metasurfaces. *Appl. Phys. Lett.* **2025**, *126*, 081701.

(60) Mamian, K. A.; Frolov, A. Y.; Popov, V. V.; Fedyanin, A. A. Transverse Magneto-Optical Kerr Effect Enhancement in Si−Ni Nanogratings by Mie and Surface Lattice Resonances. *Phys. Met. Metallogr.* **2024**, *125*, 118−123.

(61) Singh, I.; Nayyar, V. Lateral displacement of a light beam at a ferrite interface. *J. Appl. Phys.* **1991**, *69*, 7820−7824.

(62) Tang, T.; Qin, J.; Xie, J.; Deng, L.; Bi, L. Magneto-optical Goos-Hänchen effect in a prism-waveguide coupling structure. *Opt. Express* **2014**, *22*, 27042−27055.

(63) Yu, W.; Sun, H.; Gao, L. Magnetic control of Goos-Hänchen shifts in a yttrium-iron-garnet film. *Sci. Rep.* **2017**, *7* (1), 45866.

(64) Tang, T.; Li, J.; Luo, L.; Shen, J.; Li, C.; Qin, J.; Bi, L.; Hou, J. Weak measurement of magneto-optical Goos-Hänchen effect. *Opt. Express* **2019**, *27*, 17638−17647.

(65) Ma, H.; Ju, C.; Xi, X.; Wu, R.-X. Nonreciprocal Goos-Hänchen shift by topological edge states of a magnetic photonic crystal. *Opt. Express* **2020**, *28*, 19916−19925.

(66) Dadoenkova, Y. S.; Bentivegna, F. F. L.; Dadoenkova, N. N.; Lyubchanskii, I. L.; Lee, Y. P. Influence of misfit strain on the Goos-Hänchen shift upon reflection from a magnetic film on a nonmagnetic substrate. *J. Opt. Soc. Am. B* **2016**, *33*, 393−404.

(67) Dadoenkova, Y. S.; Bentivegna, F. F. L.; Dadoenkova, N. N.; Petrov, R. V.; Lyubchanskii, I. L.; Bichurin, M. I. Controlling the Goos-Hänchen shift with external electric and magnetic fields in an electro-optic/magneto-electric heterostructure. *J. Appl. Phys.* **2016**, *119*, 203101.

(68) Huang, Y.; Tang, G.; Chen, J.; Li, Z.-Y.; Liang, W. Adjustable enhanced Goos-Hänchen shift in a magneto-optic photonic crystal waveguide. *Opt. Express* **2022**, *30*, 36478−36488.

(69) Sun, Y.; Zhang, Z.; Zhang, J.; Yang, C.; Zhuang, C.; Deng, D. Magneto-optical Goos-Hänchen shift in uniaxial anisotropic epsilon-near-zero metamaterials. *J. Phys. D: Appl. Phys.* **2025**, *58*, 035107.

(70) Luo, M. Goos-Hänchen shift of a normally incident beam on a magneto-optical metagrating. *Phys. Rev. B* **2026**, *113* (3), 035433.

(71) Makarova, A. V.; Nerovnaya, A. A.; Gulkin, D. N.; Popov, V. V.; Frolov, A. Y.; Fedyanin, A. A. Goos−Hänchen Shift Spatially Resolves Magneto-Optical Kerr Effect Enhancement in Magnetoplasmonic Crystals. *ACS Photonics* **2024**, *11*, 1619−1626.

(72) Inoue, M.; Arai, K.; Fujii, T.; Abe, M. One-dimensional magnetophotonic crystals. *J. Appl. Phys.* **1999**, *85*, 5768−5770.

(73) Inoue, M.; Arai, K.; Fujii, T.; Abe, M. Magneto-optical properties of one-dimensional photonic crystals composed of magnetic and dielectric layers. *J. Appl. Phys.* **1998**, *83*, 6768−6770.

(74) Inoue, M.; Fujikawa, R.; Baryshev, A.; Khanikaev, A.; Lim, P. B.; Uchida, H.; Aktsipetrov, O.; Fedyanin, A.; Murzina, T.;

Granovsky, A. Magnetophotonic crystals. *J. Phys. D: Appl. Phys.* **2006**, *39*, R151.
(75) *Magnetophotonics: from theory to applications*; Inoue, M.; Levy, M.; Baryshev, A. V. Eds.; Springer Science & Business Media, 2013.
(76) Vinogradov, A. P.; Dorofeenko, A. V.; Merzlikin, A. M.; Lisyansky, A. A. Surface states in photonic crystals. *Phys.-Usp.* **2010**, *53*, 243.
(77) Romodina, M. N.; Soboleva, I. V.; Fedyanin, A. A. Magneto-optical switching of Bloch surface waves in magnetophotonic crystals. *J. Magn. Magn. Mater.* **2016**, *415*, 82−86.
(78) Romodina, M. N.; Soboleva, I. V.; Musorin, A. I.; Nakamura, Y.; Inoue, M.; Fedyanin, A. A. Bloch-surface-wave-induced Fano resonance in magnetophotonic crystals. *Phys. Rev. B* **2017**, *96*, 081401.
(79) Fedyanin, A. A.; Aktsipetrov, O. A.; Kobayashi, D.; Nishimura, K.; Uchida, H.; Inoue, M. Enhanced Faraday and nonlinear magneto-optical Kerr effects in magnetophotonic crystals. *J. Magn. Magn. Mater.* **2004**, *282*, 256−259.
(80) Ignatyeva, D.; Kapralov, P.; Golovko, P.; Shilina, P.; Khramova, A.; Sekatskii, S.; Nur-E-Alam, M.; Alameh, K.; Vasiliev, M.; Kalish, A.; Belotelov, V. Sensing of Surface and Bulk Refractive Index Using Magnetophotonic Crystal with Hybrid Magneto-Optical Response. *Sensors* **2021**, *21*, 1984.
(81) *Lumerical FDTD Solutions*; ANSYS, Inc., http://www.ansys.com/products/optics/fdtd, (accessed 2022.02.02).
(82) Hansen, P.; Krumme, J. P. Magnetic and magneto-optical properties of garnet films. *Thin Solid Films* **1984**, *114*, 69−107.

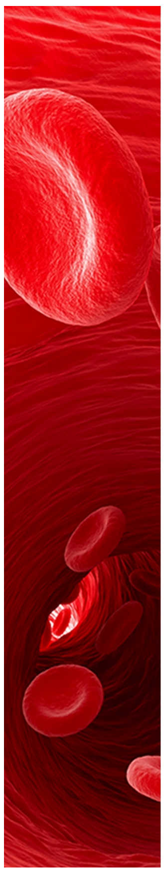

https://doi.org/10.1021/acsphotonics.6c00737
ACS Photonics 2026, 13, 3501−3508